RSC Advances

PAPER

Cite this: *RSC Adv.*, 2019, **9**, 9968

Poly(norepinephrine)-coated FeOOH nanoparticles as carriers of artemisinin for cancer photothermal-chemical combination therapy†

Zi He,‡[a] Huiling Su,‡[a] Yuqing Shen,[b] Wei Shi, *[a] Xin Liu,[a] Yang Liu,[a] Fuhui Zhang,[b] Yansheng Zhang,[b] Yanan Sun[a] and Dongtao Ge*[a]

The photothermal-chemical combination therapy is a promising approach for cancer treatment, however, chemotherapy often causes severe toxic and side effects on normal tissues. Herein, tumor-specific FeOOH@PNE-Art nanoparticles were fabricated *via* coating poly(norepinephrine) (PNE) on FeOOH nanoparticles, followed by loading of artemisinin (Art). The as-prepared nanoparticles exhibited excellent biocompatibility, strong near-infrared (NIR) absorbance and pH-responsive synchronous release of Art and iron ions. The released iron ions could not only supply iron ions in cancer cells which mediate endoperoxide bridge cleavage of Art and generate reactive oxygen species (ROS), but also react with H_2O_2 at tumour sites *via* the Fenton reaction and produce hydroxyl radicals, inducing a tumour-specific killing. Moreover, owing to the synchronous release of Art and iron ions as well as the low leakage of iron ions, FeOOH@PNE-Art nanoparticles showed extremely low toxicity to normal tissue. Under NIR light irradiation, the tumours in FeOOH@PNE-Art injected mice were thoroughly eliminated after 7 days of treatment and no tumour recurrence was found 30 days after treatment, manifesting very high efficacy of combination therapy.

Received 20th February 2019
Accepted 20th March 2019

DOI: 10.1039/c9ra01289c

rsc.li/rsc-advances

Introduction

Among the various cancer therapies, chemotherapy is the most commonly adopted treatment. However, it suffers from low therapeutic efficiency, drug resistance and severe adverse effects.[1,2] The recently developed photothermal-chemical combination therapy exhibited great potential in cancer therapy,[3] since it not only integrated two modes of cancer treatment, but also enhanced drug toxicity to cancer cells *via* elevated temperature from photothermal therapy (PTT) at tumour sites.[4] Moreover, PTT-induced hyperthermia could enhance tumor cell uptake of nanocarriers and accelerate drug release from nanocarriers.[5] Although favorable therapeutic efficacy was achieved by the combination of PTT and chemotherapy, the problem of strong side effects of chemotherapy on normal tissues remains.

Artemisinin (Art), a natural plant drug, is extracted from the herb *Artemisia annua* and has been widely used as an antimalaria medicament.[6] Recent studies revealed that Art can also be used for cancer therapy, which inhibits angiogenesis, blocks the metastasis and suppresses proliferation of cancer cells.[7–10] The anticancer mechanism of Art is that the peroxy bridge in Art would be broken in the presence of Fe^{2+}, leading to releasing of free radicals and reactive oxygen species (ROS), which would cause cellular oxidative damage.[11–13] Accordingly, Art is more toxic to cancer cells for the reason that there are more ferrous ion in tumour cells than normal cells.[14,15] However, the limited iron supply in tumour cells and intrinsic hydrophobicity of Art obstructed clinical application of Art as a chemotherapeutic drug.[16–19] Nevertheless, these problems can be solved by developing suitable Fe-contained nanocarriers. Recently, many nanocarriers containing iron sources for delivery of Art, such as Fe_3O_4 and metal–organic-frameworks (MOFs) nanoparticles, have been developed.[20–23] These nanoparticles acquired a high drug loading efficiency, provided the sufficient iron ion, and greatly enhanced the therapeutic efficacy of Art. However, the excessive iron ion supplied by these nanoparticles not only has strong side effects, but also would increase the risk of normal tissue being attacked by free radicals, leading to poor effect of chemotherapy. Compared with Fe_3O_4 and MOFs nanoparticles, FeOOH nanoparticles have lower leakage rate of iron ion. Moreover, fusiform FeOOH nanoparticles are more easily uptaken by cancer cells, since they could penetrate tumours *via* the vessel pores and reach the tumour cells more rapidly.[24–26] Therefore, using FeOOH nanoparticles as carrier for Art would be conducive to enhancing uptake efficiency of drug in tumour cells and reducing damage to normal tissues. However, the poor

[a]*Key Laboratory of Biomedical Engineering of Fujian Province University/Research Center of Biomedical Engineering of Xiamen, Department of Biomaterials, College of Materials, Xiamen University, Xiamen 361005, China. E-mail: shiwei@xmu.edu.cn; gedt@xmu.edu.cn; Fax: +86 592 2188502; Tel: +86 592 2188502*

[b]*Xiamen Maternal and Child Health Hospital, Xiamen 361003, China*

† Electronic supplementary information (ESI) available. See DOI: 10.1039/c9ra01289c

‡ These authors contributed equally to this work.

stability in physiological environments restricted the application of FeOOH nanoparticles as drug carriers.

Inspired from robust adhesion of mussels, catecholamine-based surface chemistry provided a promising material-independent functionalization strategy for forming polymer coatings.[27–32] Norepinephrine (NE) as catechol molecule is a dopamine derivative with an additional hydroxyl group, which can generate a poly(norepinephrine) (PNE) adherent coating on the substrate surfaces *via* oxidative polymerization in alkaline environment.[33,34] Compared with polydopamine, PNE presents a more uniform, thinner and smooth coating, due to its controllable polymerization process.[35–38] Therefore, it is more suitable for the modification of nanomaterials.[39–41] Moreover, owing to the similar conjugate structures with polydopamine, PNE promises to be a potential photothermal agent. However, to the best of our knowledge, the photothermal performance of PNE has not been reported so far.

In this paper, fusiform FeOOH nanoparticles were selected as carrier of Art to supply iron sources. To enhance the dispersity of nanoparticles and load drug, FeOOH nanoparticles were functionalised with PNE by polymerization of NE under alkaline condition, as shown in Scheme 1. The as-fabricated nanoparticles (FeOOH@PNE-Art) exhibited excellent biocompatibility, high near-infrared (NIR) absorbance and synchronous release of Art and iron ions. Besides Art-mediated chemotherapy, the released iron ion from FeOOH@PNE-Art also triggered hydroxyl radical-based chemotherapy *via* Fenton reaction, due to the overexpressed H_2O_2 at tumour sites. The tumour-specific nanoparticles synthesized in this paper not only solve the problems of poor curative effect and high side-effects of chemotherapy, but also achieve complete eradication of the tumor by combining PTT and chemotherapy, showing prominent application prospect.

Experimental section

Materials

Artemisinin (Art) was purchased from Beijing Suo Laibao Technology Co., Ltd. Norepinephrine hydrochloride (NE), 1,3-diphenylisobenzofuran (DPBF), 5,5-dimethyl-1-pyrroline-*N*-oxide (DMPO) and dichlorofluorescein-diacetate (DCFH-DA) were obtained from Sigma-Aldrich Co., Ltd. Dulbecco's modified Eagle's medium (DMEM), Roswell Park Memorial Institute (RPMI) 1640 medium and fetal calf serum (FBS) were acquired from Life Technologies Co., Ltd. All solvents and reagents were obtained commercially and used without further purification.

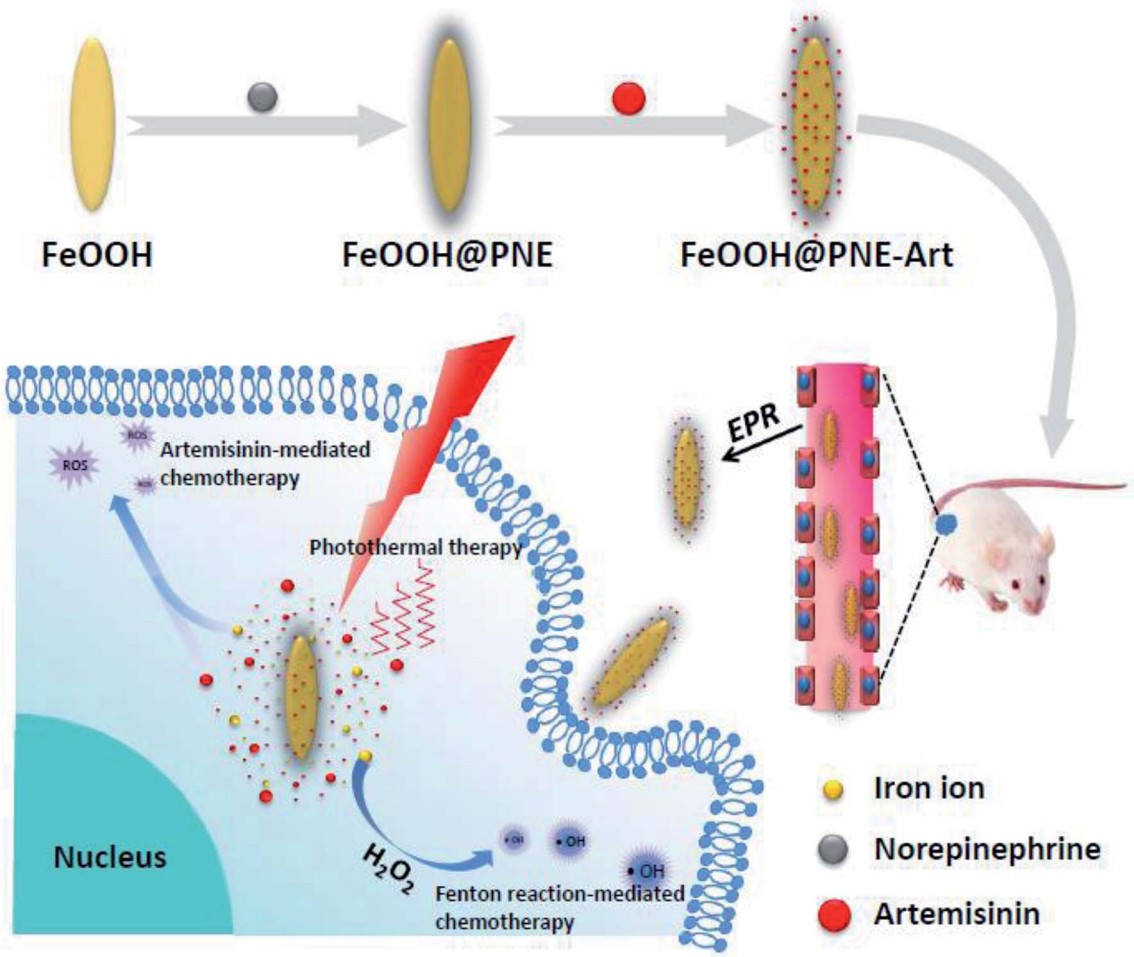

Scheme 1 Illustration of the fabrication and *in vivo* anticancer application of FeOOH@PNE-Art nanoparticles.

L929 mouse fibroblasts (L929 cells) and mouse breast cancer 4T1 cells (4T1 cells) were bought from the Cell Center of Basic Medical Sciences Chinese Academy of Medical Sciences.

Characterization

Transmission electron microscopy (TEM) was carried out on a JEOL JEM-1400 to observe the morphology of nanoparticles. X-ray diffraction (XRD) analysis was carried out on a 2.2 kW X-ray diffractometer using Cu (60 kV, 55 mA) radiation. A Malvern Zetasizer Nano ZS (Model: ZEN 3600) was used to determine the size and zeta potential of products. The Fourier transform infrared spectroscopy (FTIR) spectra were collected by a Nicolet iS10 FTIR spectrometer with DTGS detector. Scans over wavelengths between 500 and 4000 cm^{-1} were selected with a resolution of 2 cm^{-1} and averaging 32 scans for each spectrum. A SHIMADZU UV-1750 spectrophotometer was applied for UV-Vis-NIR absorption spectra. Iron ion concentration was measured by inductively coupled plasma mass spectrometry (ICP-MS, Agilent 7500ce). A laser device (F2419V) and an infrared thermal imager (FOTRIC 220) were applied for the detection of photothermal performance.

Synthesis of FeOOH@PNE

FeOOH nanoparticles were prepared by hydrothermal method.[42] Briefly, $FeCl_3 \cdot 6H_2O$ (1.16 g) was dissolved in 200 mL deionized water to form a clear yellow solution, followed by stirring mechanically for 12 h at 55 °C until the solution became turbid. The FeOOH nanoparticles were collected by centrifugation (14 500 rpm, 20 min), washed just once by water, then redispersed in water and kept at 4 °C for further use.

350 mg NE was dissolved in 120 mL Tris buffer solution (10 mM, pH 8.5), followed by adding 1 mL FeOOH nanoparticles aqueous dispersions (30 mg mL^{-1}). The mixture was stirred under room temperature for 48 h until the color of solution changed from orange to brownish black. Finally, the obtained product (FeOOH@PNE) was stored in water at 4 °C after centrifugation (16 000 rpm, 20 min) and washing three times with deionized water.

Photothermal performance evaluation

To study the photothermal performance of the nanoparticles, FeOOH@PNE nanoparticle aqueous dispersions with different concentration were exposed on an 808 nm laser with the power density of 2 W cm^{-2} for 8 min. The temperature of the solution was recorded by an electronic contact thermometer (Testo AG 925) every minute. In a same way, the photothermal stability of the nanoparticles was investigated under the irradiation of an 808 nm laser (2 W cm^{-2}) for 10 min, then the laser was turned off until the sample returns to room temperature and the temperature was recorded continuously at each iteration.

Art loading and *in vitro* release

1 mL Art solution (dissolved in ethanol) with different concentrations (0.05, 0.1, 0.2, 0.3, 0.4, 0.5 mg mL^{-1}) was mixed with 4 mL FeOOH@PNE (0.5 mg mL^{-1}) for drug loading. The mixture was sealed and stirred magnetically for 12 h, followed by removing ethanol *via* evaporation. Then the solution was centrifuged (16 000 rpm, 20 min) and washed once by water. The supernatant after centrifugation was collected for the detection of Art content. To measure Art concentration, 95% ethanol and 0.2% NaOH were added into the Art solution followed by hydrolyzing for 30 min at 55 °C. After cooling rapidly with ice and returning to room temperature, the absorbance of the solution was measured at 290 nm.[43]

To evaluate the drug release of the nanoparticles, 1 mL 10 mg mL^{-1} FeOOH@PNE-Art was dispersed in 4 mL PBS (pH = 7.4, 6.5 and 5.0) and incubated at 37 °C with rotating speed of 100 rpm in an oscillation incubator. At specified time point, the solution was irradiated with an 808 nm laser (2 W cm^{-2}) for 10 min or not, and then centrifuged at 16 000 rpm for 20 min. 4 mL of each supernatant solution were collected and the same volume of PBS was supplied to the residual solution of the FeOOH@PNA-Art. To evaluate the released amount of Art, 0.2% NaOH solution was added into the collected supernatant solution, and the solution was hydrolyzed at 55 °C for 30 min followed by measuring the absorbance at 290 nm.

Cytotoxicity assessments

L929 and 4T1 cells were incubated in DMEM and RPMI 1640 medium at 37 °C under a CO_2 (5%) humid atmosphere, respectively, and the medium supplement contains 1% penicillin/streptomycin and 10% FBS.

To evaluate cytotoxicity of FeOOH@PNE, 4T1 and L929 cells were plated in 96-well plates (1×10^4 per well), respectively, and allowed to culture for 24 h. Then cells were cocultured with different concentrations of FeOOH@PNE for 24 h. After washing with PBS, the cells were treated with 100 μL of MTT solution (1 mg mL^{-1}) for 4 h. The MTT solution was subsequently replaced by 200 μL DMSO followed by incubating for 30 min with mild concussion. At last, the absorbance was measured at 490 nm by a microplate reader (TECAN, infinite M200 PRO).

For photothermal therapy *in vitro*, 4T1 cells were dispersed in culture medium with or without H_2O_2, followed by cultivating for 4 h after seeding in 96-well pates at 1×10^4 cells per well. An 808 nm laser (2 W cm^{-2}) was applied to irradiate the cells for 5 min with the power density of 2 W cm^{-2} after the addition of FeOOH@PNE with different concentrations, followed by further incubation for 24 h at 37 °C in 5% CO_2 before MTT assay. For chemotherapeutic efficacy, after seeding the cells in 96-well plates (1×10^4 per well) with or without H_2O_2 and cultivating for 24 h, 100 μL different concentrations of free Art, PNE-Art and FeOOH@PNE-Art were added respectively, followed by coculturing for another 24 h and MTT assay was performed to detect the cells activity. For combination therapy, after cell seeding with or without the existence of H_2O_2, FeOOH@PNE-Art with different concentrations was added for coincubation for 4 h at 37 °C in 5% CO_2. After irradiating by an 808 nm laser (2 W cm^{-2}) for 5 min, the cells were continued to incubate for 24 h before MTT assay.

Cell uptake assay

To examine the cellular uptake, Rhodamine B (RhB) was used as a probe to label the FeOOH@PNE nanoparticles. Briefly, 1 mg

RhB, 1 mg NHS and 1 mg EDC were added in 5 mL water and stirred for 3 h, followed by the addition of 1 mL 10 mg mL^{-1} FeOOH@PNE to react overnight. The FeOOH@PNE-RhB was collected by centrifugation at 16 000 rpm for 20 min, and then the obtained nanoparticles were washed with deionized water until the supernatant was clear.

4T1 cells were seeded on cell slides which were put in a 24-well black plate (2×10^5 per well) and cultured for 24 h at 37 °C in 5% CO_2. Then the culture medium containing FeOOH@PNE-RhB was added to coculture for another 0.5, 2 or 4 h, followed by washing with PBS and fixing with 4% paraformaldehyde (500 μL) for about 20 min. The fluorescence was observed under a laser scanning confocal microscope (LSCM) after nuclei were stained by Hoechst 33258. The whole experiment was carried out in the dark.

ROS detection

To detect the generation of hydroxyl radical (·OH) from Fenton reaction between FeOOH and H_2O_2, 70 μL of FeOOH or FeOOH@PNE (300 μg mL^{-1}) were mixed with 20 μL of DMPO (200 mM), respectively, followed by adding 10 μL H_2O_2 (10 mM). 70 μL of above solution were transferred to an NMR tube and analyzed by the spectrometer of electron spin resonance (ESR). To study the effect of temperature on ·OH generation, methylene blue (MB) decolorization method was used by recording UV-Vis absorption spectra of 3 mL solution containing MB (6 mg mL^{-1}), $FeSO_4$ (200 μM) and H_2O_2 (1 mM) at different temperature (37, 45 and 55 °C) with UV-1750 spectrophotometer.

To test ROS generation from Art–Fe^{2+} reaction, UV-Vis absorption spectra of the ethanol solution containing ROS trapper (DPBF), Art and $FeSO_4$ with the same concentration of 100 μM was recorded by the UV-Vis spectrophotometer at different reaction time at 25 °C. The effect of temperature on ROS generation was evaluated by measuring the absorbance of the above solution at different temperature (25, 37, 45 and 55 °C) after 20 minutes of reaction.

Dichlorofluorescein-diacetate (DCFH-DA) method was carried out to measure intracellular ROS level. 1×10^5 4T1 cells were seeded on a coverslip and cultured in a 24-well plate for 12 h. Then cells were cocultured with fresh medium (as control), Art, FeOOH@PNE and FeOOH@PNE-Art with or without 0.1 mM H_2O_2 supplement for 6 h. An 808 nm laser (2 W cm^{-2}, 3 min) was used in each irradiation group before staining with 500 μL DCFH-DA (10 μM) at 37 °C for 30 min. After washing with PBS for three times, the coverslips were fixed on glass slides with the anti-fluorescence quenching sealant, followed by the observation with confocal laser scanning microscopy (CLSM, Olympus FV1000, E_x: 488 nm, E_m: 510–530 nm).

Animal model

Female BALB/c nude mice (6–8 weeks) were bought from Laboratory Animal Center of Xiamen University. Animal experiments were conducted in compliance with the guidelines the Care and Use of Laboratory Animals of Xiamen University, and were approved by the Animal Ethics Committee of Xiamen University. 4T1 cells (1×10^6) in 100 μL of PBS were subcutaneously injected into the right belly of each mouse. The tumour-bearing mice were used for experiments when the tumour size reached about 100 mm^3.

In vivo imaging

For fluorescence imaging, 4T1 tumour-bearing mice were injected with 100 μg FeOOH@PNE-RhB nanoparticles *via* tail vein, and IVIS Lumina was used for observing the distribution of nanoparticles in heart, liver, spleen, lung, kidney and tumour at predesigned time intervals.

For photothermal imaging, 4T1 tumour-bearing mice were received tail intravenous injection of PBS, FeOOH@PNE, FeOOH@PNE-Art, respectively. After 24 h, the tumour sites were irradiated with an 808 nm laser (2 W cm^{-2}) for 5 min and infrared thermal imager was used to collect date from the photothermal treatment in mice.

In vivo therapy

30 mice were divided into six groups ($n = 5$), *i.e.*, PBS, PBS + laser, free Art, FeOOH@PNE-Art, FeOOH@PNE + laser and FeOOH@PNE-Art + laser group. The tumor-bearing mice were injected with 100 μL each medicament *via* the tail vein, where the FeOOH@PNE-Art + laser group has an equivalent Art dosage (25 μg) to the Art group and has an equivalent FeOOH@PNE nanoparticles dosage (500 μg) to the FeOOH@PNE + laser group. During the treatment period, each group was injected with corresponding medicament only once. Laser groups were treated with an 808 nm laser (2 W cm^{-2}) continuously for 5 min every day in one week. The body weight and tumour volume were measured and recorded in two weeks. After the treatment for 4 days, one of tumour-bearing mice from each group was selected for dissection, and the heart, liver, spleen, lung, kidney and tumour were taken out respectively. All of the organs were fixed with 4% glutaraldehyde solution, gradiently dehydrated by alcohol, embedded in paraffin, sliced, and stained by H&E before observation.

Results and discussion

Characterization of the nanoparticles

FeOOH nanoparticles were prepared by hydrothermal method with the use of $FeCl_3 \cdot 6H_2O$ as a precursor.[42] TEM observation showed the obtained FeOOH nanoparticles were fusiform in shape, and the length and width of the nanoparticles were about 100–150 and 30 nm, respectively (Fig. 1A). XRD was used to investigate the structure of FeOOH nanoparticles (Fig. S1†). The obtained diffraction pattern was consistent with the standard card JCPDS no. 34-1266, indicating that our as-prepared FeOOH was tetragonal fibrite-type β-FeOOH. Due to excellent biocompatibility and strong adhesion, we chose PNE to modify FeOOH nanoparticles by polymerizing NE onto the surface of FeOOH nanoparticles. TEM image (Fig. 1B) showed, compared to FeOOH nanoparticles, the size and morphology of the FeOOH@PNE nanoparticles have not apparently changed. FeOOH showed hydrodynamic particles size of 85 nm

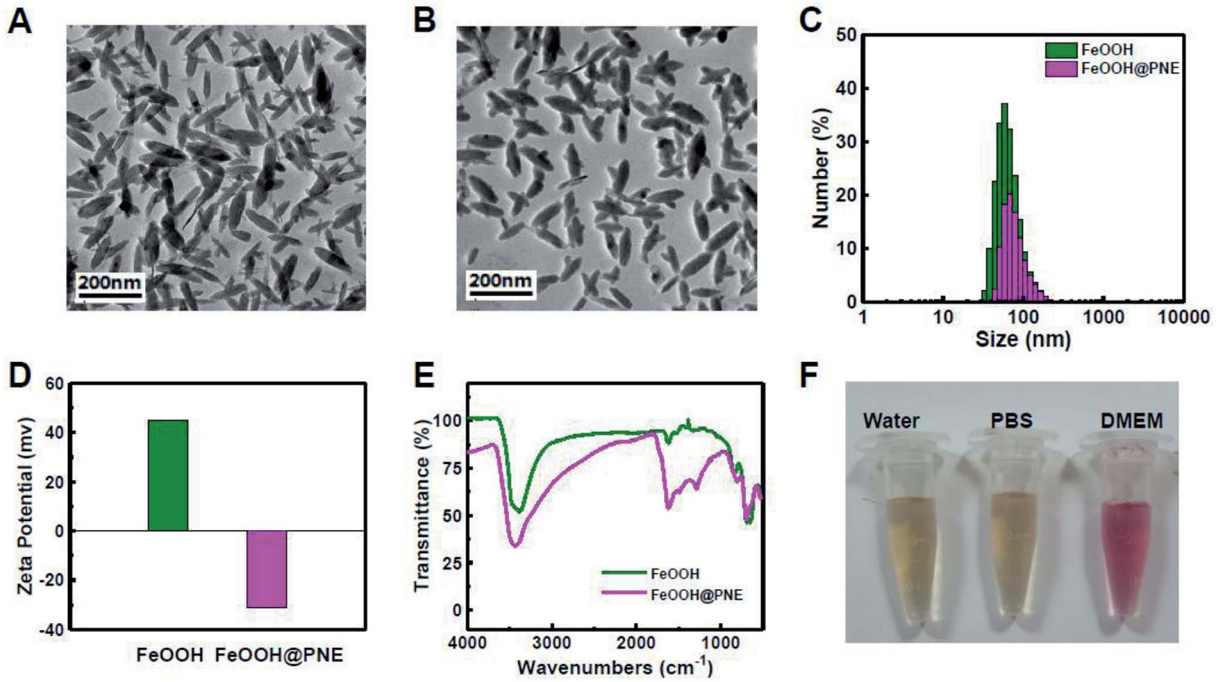

Fig. 1 The TEM images of FeOOH (A) and FeOOH@PNE (B). Size distribution (C) and zeta potential (D) of FeOOH and FeOOH@PNE. (E) The FTIR spectra of FeOOH and FeOOH@PNE. (F) The stability of FeOOH@PNE in water, PBS and cell medium (20% FBS).

(polydispersity index (PDI) = 0.108) and a zeta potential of +44.6 mV (Fig. 1C and D). After the polymerization of NE, an enlarged hydrodynamic size (122 nm) and a transformational zeta potential (−31.3 mV) were found. FTIR spectra (Fig. 1E) of FeOOH revealed that the peaks of the stretching vibration of Fe–O appear at 1640, 1400, 1100 and 895 cm^{-1}. The peaks at 1600 and 1510 cm^{-1} in FeOOH@PNE were attributed to the structure of indoline, which further confirmed the successful coating PNE onto the surface of FeOOH nanoparticles. Fig. 1F showed that FeOOH@PNE nanoparticles were evenly dispersed in water, PBS and cell medium for at least 1 week, indicating excellent physiological stability.

Detection of photothermal performance

For the requirement of PTT, photothermal agent should have the capacity to convert light energy into heat energy under the irradiation of an external NIR light source. To investigate whether the PNE can be used as photothermal coating, we first measured the UV-Vis-NIR absorption spectra of FeOOH@PNE nanoparticles (Fig. 2A). It can be clearly seen that there is not NIR adsorption for FeOOH nanoparticles. However, the FeOOH@PNE nanoparticles showed a strong NIR adsorption, and the absorption is enhanced with the increase of FeOOH@PNE nanoparticles concentration (Fig. S2†), indicating that PNE coating was a potential photothermal agent.

To investigate the effect of concentration on photothermal performance, FeOOH@PNE nanoparticles with different concentration were irradiated for 8 min by an 808 nm laser at power density of 2.0 W cm^{-2}. Fig. 2B showed that the solution temperature increased with irradiation time and the concentration of the nanoparticles. At the concentration of 200 μg mL^{-1}, the solution was warmed up to above 45 °C after irradiation for 8 min, which is higher than the tolerated temperature of cancer cells. In comparison, the pure water group (as control) only went up 2.7 °C under the same laser exposure. The effect of light dose on photothermal performance was then studied by irradiation of different power density on 200 μg mL^{-1} FeOOH@PNE nanoparticles for 8 minutes. Fig. 2C showed the temperature of the nanoparticle solutions increased with the increase of power density. The above results indicated that photothermal performance of FeOOH@PNE nanoparticles was laser power and concentration dependent. For the simulation of continuous photothermal therapy, cyclic illumination (2.0 W cm^{-2}) was applied to FeOOH@PNE nanoparticles (200 μg mL^{-1}) for 10 min followed by a break without light irradiation (Fig. 2D). After three laser irradiation on–off cycles, the temperature raising effect of nanoparticles did not change substantially, indicating that the as-prepared FeOOH@PNE nanoparticles own good photothermal stability.

Drug loading and releasing property

Art was chosen as model drug for chemotherapy and loaded onto FeOOH@PNE nanoparticles by electrostatic interaction and π–π stacking. The FTIR spectra (Fig. S3†) revealed that the stretching vibration peaks of FeOOH@PNE-Art at 1750–1753 and 1245 cm^{-1} ascribed to the C=O and C–O–C of Art, respectively, confirming that Art was loaded successfully onto FeOOH@PNE. To study the drug loading efficiency (DLE) and drug encapsulation efficiency (DEE), the FeOOH@PNE (0.5 mg mL^{-1}) was added to Art solutions of various concentrations. The DLE increased with the increase of the Art concentration, while

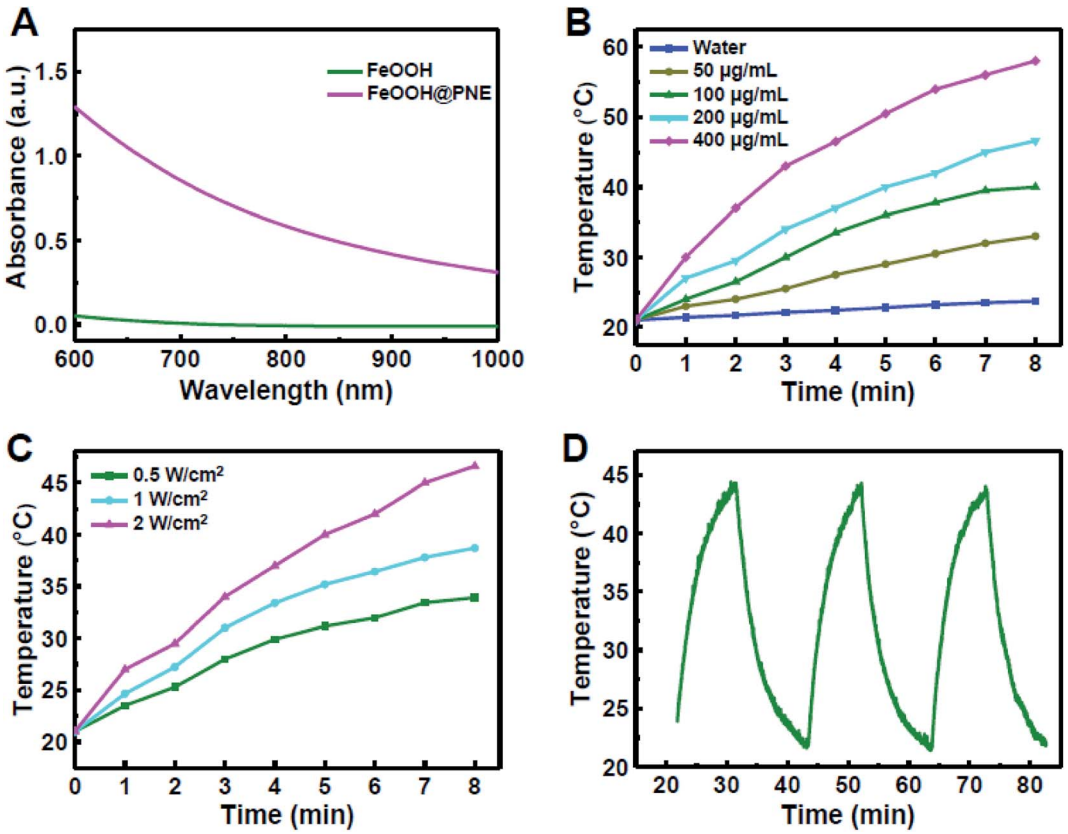

Fig. 2 (A) The UV-Vis-NIR absorption spectra of FeOOH and FeOOH@PNE. (B) The photothermal temperature curves of different concentrations of FeOOH@PNE under an 808 nm laser (2 W cm^{-2}) for 8 min and (C) temperature elevation of FeOOH@PNE (200 μg mL^{-1}) by laser irradiation (808 nm, 8 min) of different power density. (D) The temperature change curves of FeOOH@PNE nanoparticles (200 μg mL^{-1}) after multiple cycles of an 808 nm laser radiation (2 W cm^{-2} for 10 min each time).

the DEE decreased (Fig. S4†). The saturated DLE is about 5% when the concentration of Art was greater than 60 μg mL^{-1}.

To investigate the drug releasing *in vitro*, different pH conditions (7.4, 6.5 and 5.0) were chosen for simulating the physiological microenvironment of normal tissue, tumour and lysosome, respectively. The FeOOH@PNE-Art nanoparticles exhibited a relatively slower release rate and only 22.7% of Art were released within 24 h at pH 7.4 (Fig. 3A). However, higher accumulative amounts of released Art, *i.e.* 30.2% and 44.8%, were acquired at pH 6.5 and pH 5.0, respectively, which suggested that more drugs could be released in the tumour microenvironment. This phenomenon was attributed to the weakening electrostatic interaction between Art and FeOOH@PNE under lower pH level. Fig. 3A also illustrated the influence of laser irradiation (2 W cm^{-2} for 10 min) on drug release. It can be seen that Art release was enhanced under laser irradiation, and the most significant promotion of release by laser irradiation was found at pH 5.0, indicating that laser irradiation could enhance the chemotherapy efficacy of FeOOH@PNE-Art nanoparticles. To further examine the effect of laser irradiation on drug release, the solution containing FeOOH@PNE-Art was irradiated with an 808 nm laser at different power density (0.5, 1 and 2 W cm^{-2}) for 10 min. More rapid Art release was observed for solution under laser of higher power density (Fig. S5†). The above results indicated that the Art release from FeOOH@PNE-Art nanoparticles was temperature and pH dependent.

Since Art is Fe^{2+}-dependent antitumour agent, we further detected the release of iron ion from FeOOH@PNE under different pH by ICP-MS. A time and acidity-depended leaching of Fe^{3+} was observed and the amount of released Fe^{3+} at pH 5.0 was twice as much as that at pH 7.4 in 24 h (Fig. 3B). Since Fe^{3+} can be reduced to Fe^{2+} *in vivo*, this pH-responsive Art and iron ion synchronous release of the FeOOH@PNE-Art nanoparticles would reduce the side effects and enhance the antitumour efficacy of chemotherapy. Moreover, it should be pointed out that the released amount of iron ion from the FeOOH@PNE nanoparticles was about only one-tenth of that from Fe_3O_4 nanoparticles,[44] therefore our FeOOH@PNE-Art nanoparticles were expected to show a mild chemotherapeutic effect to cancer cells and extremely low toxicity to normal tissue.

Cellular uptake

Unlike routine chemotherapeutic drugs, Art kills tumour cell through the generation of ROS. Due to a short half-life and confined diffusion range of ROS,[45,46] the cellular uptake of carrier for Art should be very important to cancer treatment. To observe the cellular uptake of the nanoparticles, Rhodamine B (RhB) labeled FeOOH@PNE nanoparticles (FeOOH@PNE-RhB)

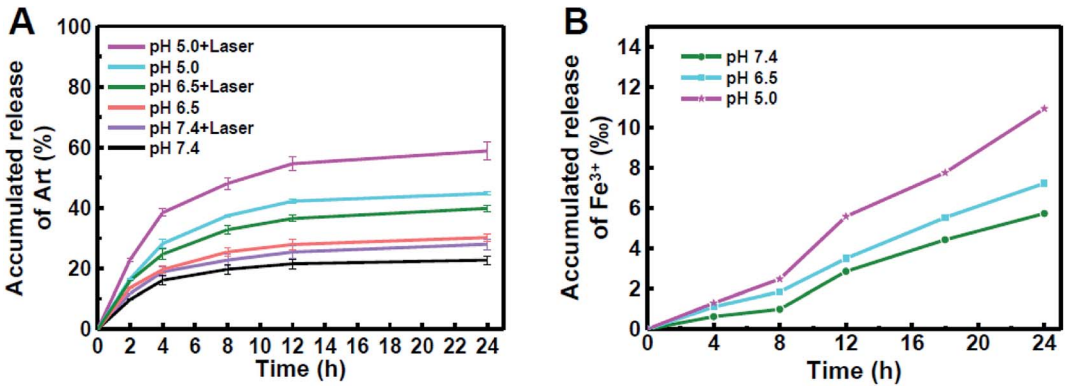

Fig. 3 The accumulated release of Art with or without laser (A) and Fe^{3+} (B) at different pH within 24 h.

were synthesized (Fig. S6†) and cocultured with 4T1 cells for 0.5, 2 and 4 h, followed by nuclear staining with Hoechst 33258. The confocal laser scanning microscope (CLSM) images (Fig. 4) showed that weak red fluorescence in the cytoplasm of the experimental groups could be observed at 0.5 h, and the fluorescence intensity significantly increased after 4 h, demonstrating the successful uptake of FeOOH@PNE nanoparticles.

ROS generation

It is well known that overexpressed H_2O_2 is a main characteristic of the tumour microenvironment (TME), which can be catalyzed by Fe-contained nanomaterials to generate reactive hydroxyl radical (·OH) *via* the Fenton reaction.[47–51] ·OH, as the most harmful ROS, would cause tumour cell damage by oxidizing lipids, proteins and DNA.[52–54] To examine the generation of ·OH of FeOOH@PNE nanoparticles in H_2O_2, electron spin resonance (ESR) analysis was carried out using DMPO as a trapper of ·OH (Fig. 5A). A clear ESR signal was observed for the both FeOOH and FeOOH@PNE in the presence of H_2O_2, confirming the production of ·OH. However, the ESR signal intensity of the FeOOH@PNE was obviously weaker than that of FeOOH, due to the coating of PNE on the FeOOH, which restrained the heterogeneous Fenton reaction between the FeOOH and H_2O_2. Then we investigated the effect of temperature on Fenton reaction by measuring the generation of ·OH at 37, 45 and 55 °C *via* methylene blue (MB) decolorization method. As shown in Fig. 5B, the decreased absorbance at higher temperature suggested the generation of a large number of ·OH which caused more degradation of MB.

To examine the ROS generation in the presence of iron ion and Art, we selected DPBF as ROS trapper, which can be oxidized by ROS. As shown in Fig. 5C, after incubating DPBF with Art and Fe^{2+}, the absorbance at 412 nm decreased with the

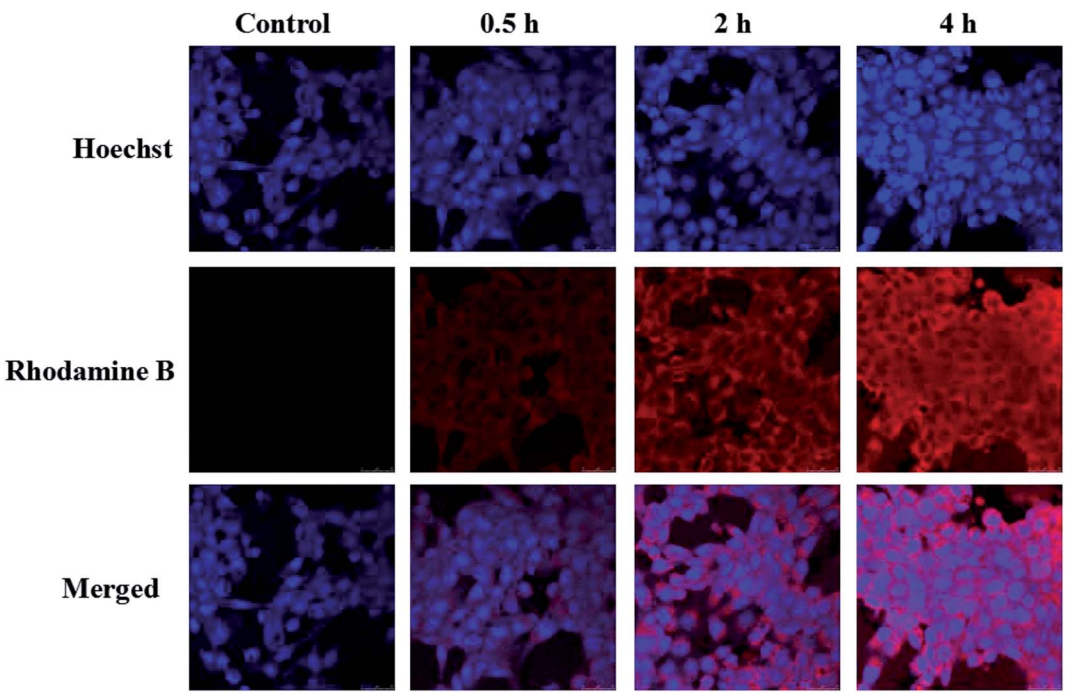

Fig. 4 The CLSM of 4T1 cells after incubation with FeOOH@PNE-RhB nanoparticles at 0.5, 2 and 4 h.

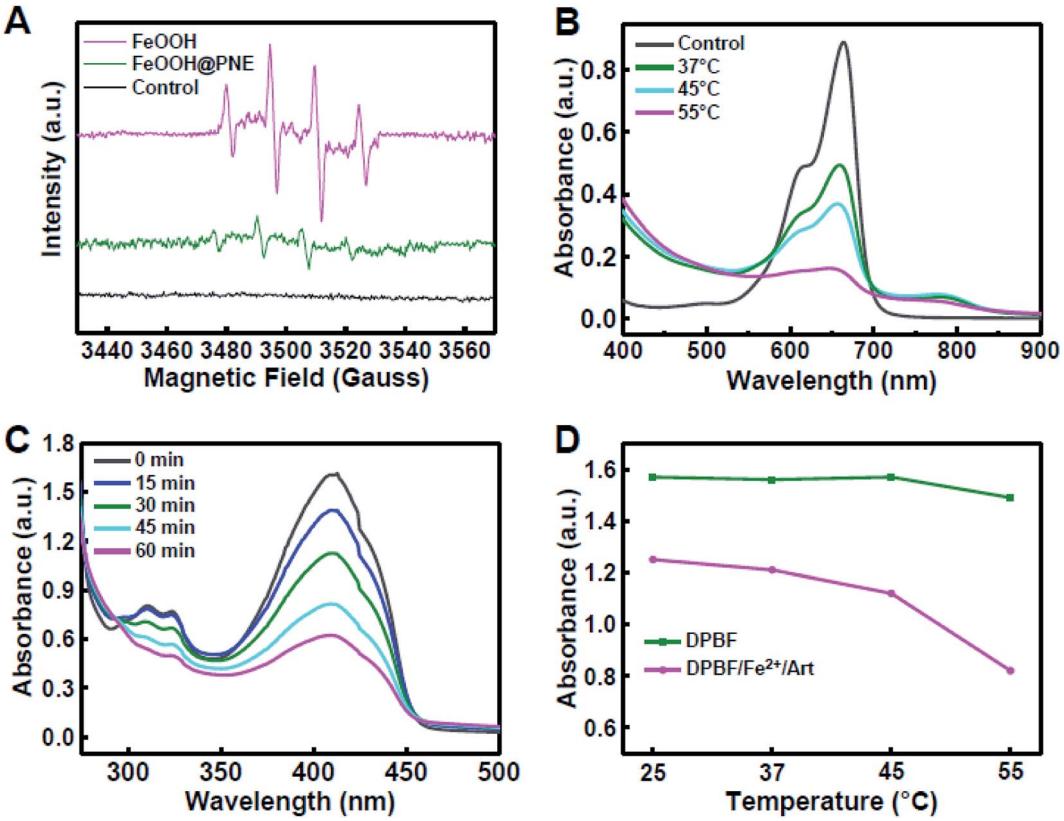

Fig. 5 (A) EPR spectra of FeOOH and FeOOH@PNE with DMPO as the spin trap. (B) Absorption spectra of MB after 1 min degradation with Fe^{2+} and H_2O_2 supplement at different temperatures. (C) Absorption spectra of DPBF upon the presence of Fe^{2+} and Art at 0, 15, 30, 45, and 60 min. (D) Comparison of the decay rate of DPBF with or without the adding of Fe^{2+} and Art at different temperatures.

increase of incubation time, demonstrating the generation of ROS. To study the effect of temperature on Art and iron ion mediated ROS generation, the solution containing DPBF, ART and Fe^{2+} was kept at 25, 37, 45, and 55 °C for 20 min, respectively. The absorbance of the solution at 412 nm decreased with the increase of reaction temperature, indicating that the elevating temperature accelerated cleavage of the endoperoxide bridge of Art by Fe^{2+} (Fig. 5D). Therefore, both Art and Fenton reaction-mediated ROS generation could be enhanced *via* photothermal effect caused by FeOOH@PNE-Art nanoparticles under laser irradiation.

Fluorescent probe DCFH-DA was used to investigate the intracellular ROS production. As shown in Fig. 6, only negligible green fluorescence was observed in control, Art and FeOOH@PNE groups, likely due to the intracellular ROS and iron ion. No obviously fluorescence change could be observed in control and Art groups after irradiation and H_2O_2 supplement alone or together. However, the intracellular fluorescence enhanced with the addition of H_2O_2 in FeOOH@PNE group, which may be attribute to the generation of ·OH by Fenton reaction. Further, laser irradiation promoted more ROS production, demonstrating that heating effect caused by laser strengthened the Fenton reaction. Besides, compared with Art group, FeOOH@PNE-Art group exhibited an obvious enhancement of fluorescence in 4T1 cells, indicating the ROS generation by interaction between exogenous iron ions and Art. Similarly, laser irradiation significant motivated the generation of ROS by breakage of peroxy bridge in Art. It is worth noting that the strongest fluorescence was observed in FeOOH@PNE-Art + laser + H_2O_2 group. This may be due to the fact that in addition to the ROS produced by reaction of Art and iron ions, extra H_2O_2 supplement reacts with exogenous iron ions to form more ROS (·OH). In addition, photothermal effect further facilitated the ROS generation.

In vitro therapeutic efficiency

To examine the cell toxicity, 4T1 mammary tumour cells and fibroblast L929 were incubated with FeOOH@PNE followed by a standard MTT assay. No obvious toxicity was found to both 4T1 and L929 cells even at a high FeOOH@PNE nanoparticles concentration of 500 μg mL^{-1}, indicating that FeOOH@PNE owns low cytotoxicity and excellent biocompatibility (Fig. S7†). We then studied the photothermal and chemotherapy efficacy of the as-prepared nanoparticles *in vitro*. After incubation with FeOOH@PNE for 24 h, irradiation groups were exposed to an 808 nm laser for 5 min with the power of 2 W cm^{-2}. As shown in Fig. 7A, it was obvious that cells irradiated with laser only did not show any reduction in cell viability and a concentration-dependent photothermal toxicity was observed. About 50% of the cells survived at a concentration of 300 μg mL^{-1} and approximately 70% of cancer cells were killed when the concentration is up to 500 μg mL^{-1}, demonstrating that FeOOH@PNE possesses a mild PTT effect. Then, the chemical

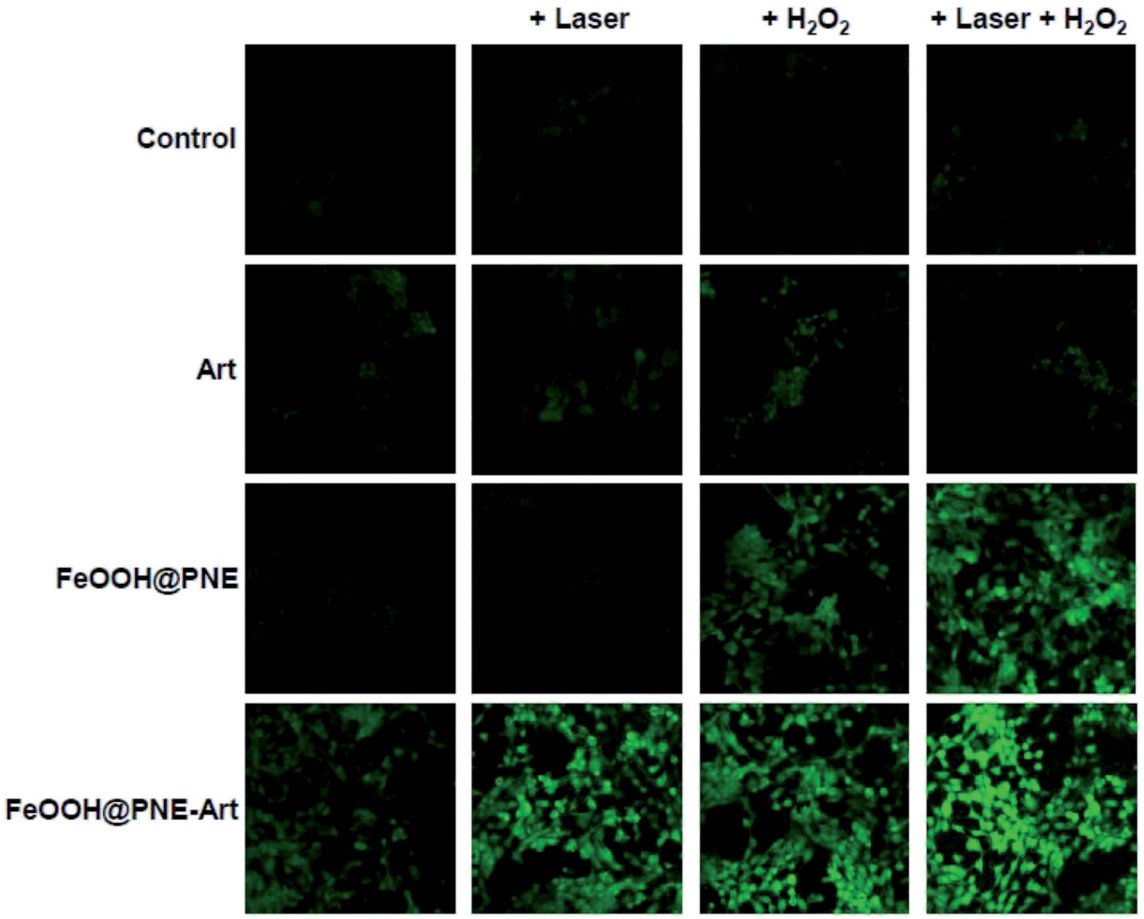

Fig. 6 Laser scanning confocal microscopy (LSCM) of intracellular Fe^{2+}-mediated and heat-induced ROS generation.

cytotoxicity was investigated by incubating 4T1 cells with free Art and FeOOH@PNE-Art of various concentrations for 24 h (Fig. 7B). A dose-dependent cytotoxicity was observed for both free Art and FeOOH@PNE-Art groups. The cytotoxicity of free Art group was very feeble within the given concentration range, due to low concentrations of intracellular iron ions. Compared with the free Art group, the FeOOH@PNE-Art group exhibited an obvious decrease in cell viability. For example, only 22% of cells were killed by free Art (25 μg mL^{-1}), while the FeOOH@PNE-Art group acquired a higher mortality of cells (50%) at the same Art concentration. The enhanced cytotoxicity was mainly attributed to Art and iron ions synchronous release from FeOOH@PNE-Art, generating more local ROS in 4T1 cells.

For combination therapy, after coculturing with FeOOH@PNE-Art of different concentrations for 24 h, 4T1 cancer cells were exposed on an 808 nm laser (2 W cm^{-2}) for 5 min, followed by a standard MTT assay. As is shown in Fig. 7C, a concentration-dependent toxicity was observed for all groups. Cellular activity in the combined treatment group (FeOOH@PNE-Art + laser) was obviously lower than the group of chemotherapy alone (FeOOH@PNE-Art) or PTT alone (FeOOH@PNE + laser). When the concentration of FeOOH@PNE-Art was 500 μg mL^{-1}, the cell viability of FeOOH@PNE-Art + laser group was about 16%. In contrast, chemotherapy alone (FeOOH@PNE-Art) and PTT alone (FeOOH@PNE + laser) only killed 48% and 69% cells at the equivalent nanoparticle concentration, respectively. The enhanced cytotoxicity of the FeOOH@PNE-Art nanoparticles under laser irradiation can be attributed to the facilitated ROS generation resulting from heating effect.

It is well known that elevated levels of H_2O_2 is one of the characteristic biochemical features of tumour microenvironment.[55–57] To more accurately evaluate combination efficacy of chemotherapy and photothermal therapy of FeOOH@PNE-Art nanoparticles *in vitro*, exogenous 0.1 mM H_2O_2 was added into culture medium to simulate the tumour microenvironment, and various treatments on 4T1 cells with or without H_2O_2 supplemented were carried out, followed by a standard MTT assay (Fig. 7D). No significant differences in cell viability were observed in Art group with or without H_2O_2 supplemented, indicating that 0.1 mM H_2O_2 have little effect on the treatment effect of Art. The FeOOH@PNE nanoparticles exhibited slight toxicity to 4T1 cells with addition of H_2O_2, indicating that intracellular Fenton reaction between the iron ion and H_2O_2 was triggered. Due to the low leakage of iron ion, the produced ·OH presented the mild killing of tumour cells. This weak Fenton reaction effect was also demonstrated in FeOOH@PNE-Art group with and without H_2O_2 supplemented. After laser irradiation to the cells, as shown in FeOOH@PNE + laser group with and without H_2O_2 supplemented, an enhanced Fenton

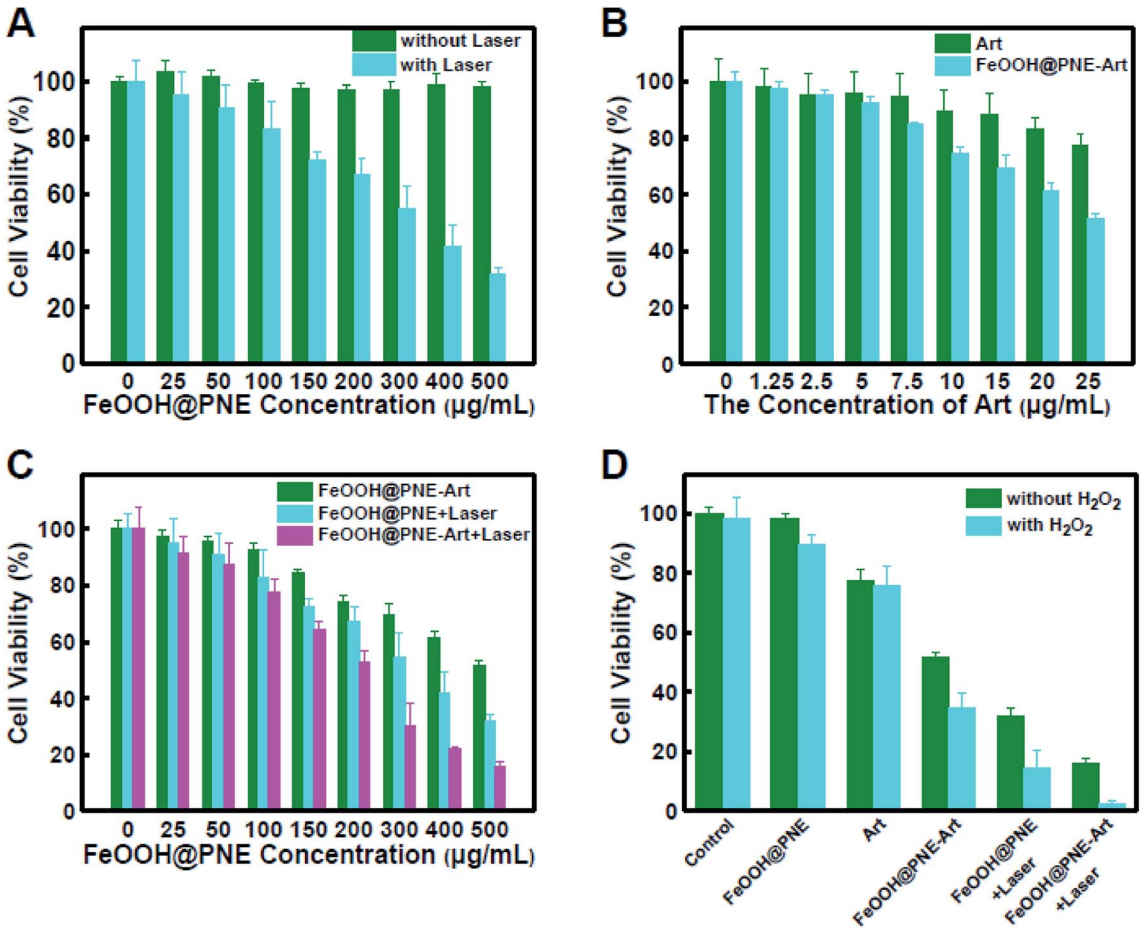

Fig. 7 (A) Cell viabilities of 4T1 cells treated with different concentrations of FeOOH@PNE nanoparticles with or without 5 min of NIR irradiation (2.0 W cm^{-2}, 808 nm). (B) Viabilities of 4T1 cells treated with different concentrations of Art and FeOOH@PNE for 24 h. (C) Cell viabilities of 4T1 cells treated with different concentrations of FeOOH@PNE and FeOOH@PNE-Art with or without 5 min of NIR irradiation (2.0 W cm^{-2}, 808 nm). (D) Cell viabilities profiles of 4T1 cells treated with Art, FeOOH@PNE and FeOOH@PNE-Art with or without addition of H_2O_2 under 5 min of NIR irradiation (2.0 W cm^{-2}, 808 nm).

reaction efficacy was found. The cell viability was greatly decreased from 32% in the absence of exogenous H_2O_2 to 14% in the presence of exogenous H_2O_2. It was mainly because heating effect strengthened Fenton reaction and promoted the generation of ·OH. More interestingly, by adding exogenous H_2O_2, the cell activity of FeOOH@PNE-Art + laser group significantly reduced from 16% to 1%, indicating that Fenton reaction further promoted the combined treatment efficiency. It should be pointed out that, although chemotherapy alone based on Fenton reaction between FeOOH and H_2O_2,

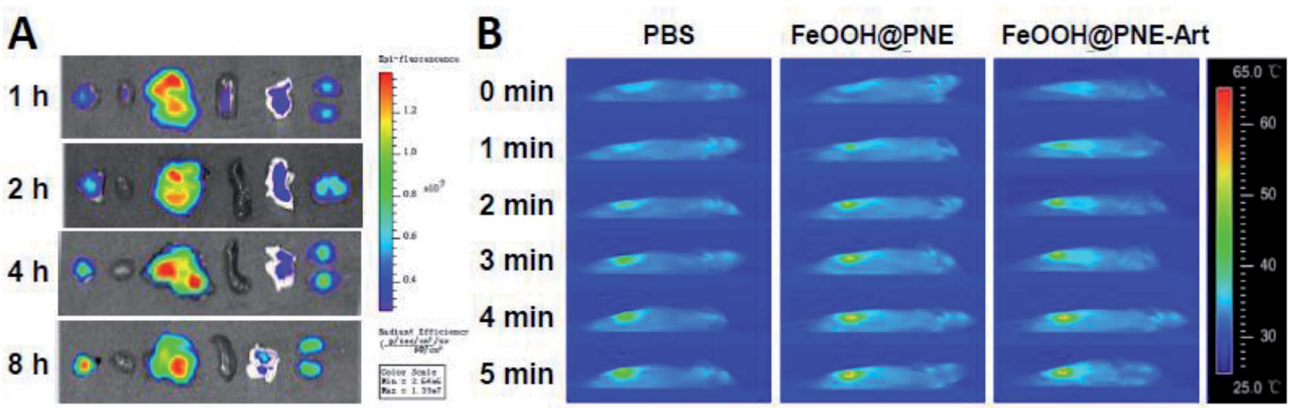

Fig. 8 (A) *Ex vivo* fluorescent images of tumours and major oranges excised from sacrificed mice after 1, 2, 4 and 8 h post-injection with FeOOH@PNE-RhB nanoparticles. (B) The photothermal image of 4T1 tumour-bearing mice recorded by the infrared camera under an 808 nm laser (2.0 W cm^{-2}) irradiation.

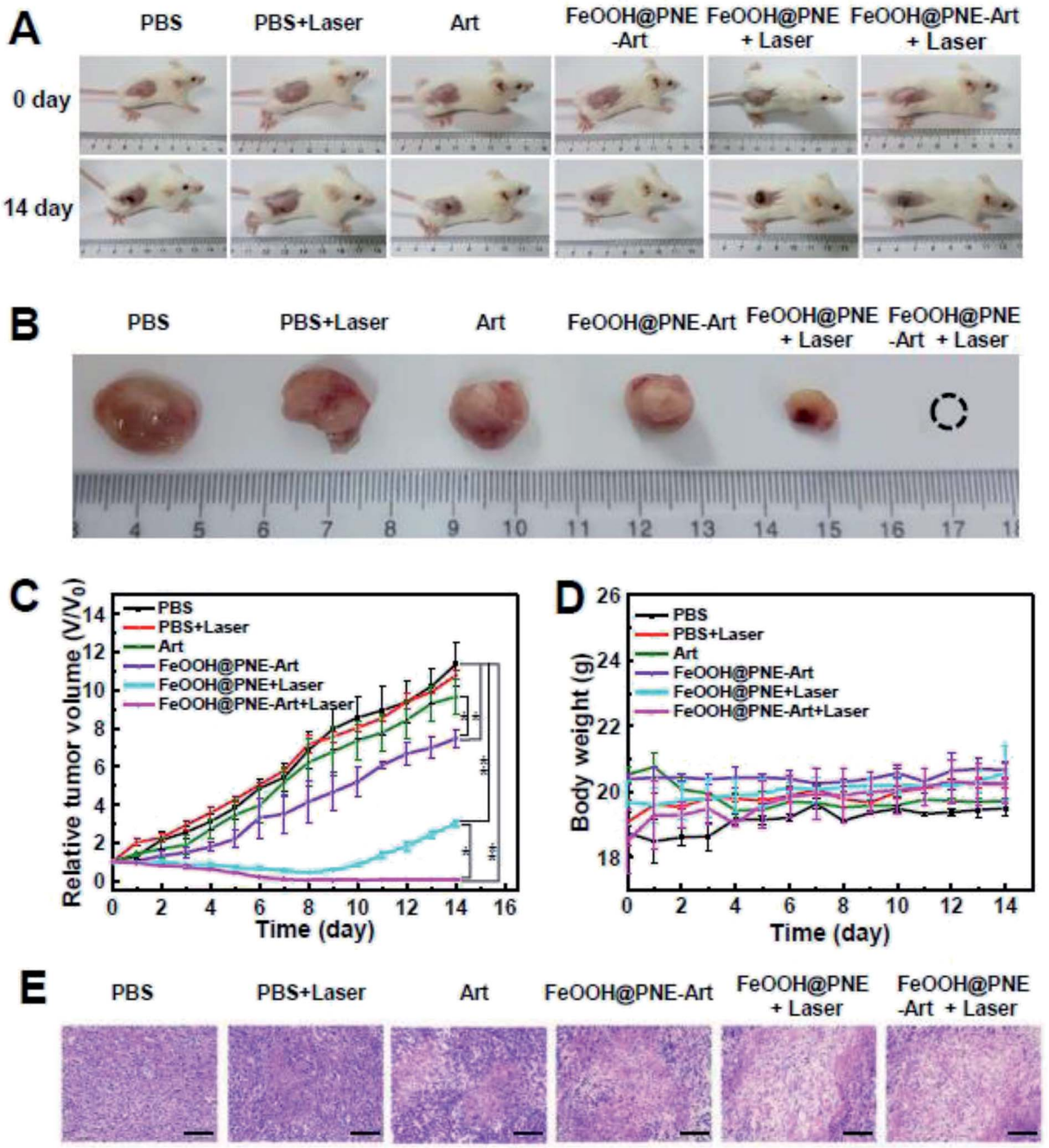

Fig. 9 (A) The digital photos of mice before and after different treatment for 14 days. (B) The digital photos of tumour tissues obtained from different treatment groups. The tumours were harvested from the mice 14 days after treatment. (C) Tumour growth curves of different groups after various treatments. (D) The body weight of mice with various treatment. (E) H&E stained slices of tumour tissues obtained from different treatment groups (scale bar, 100 μm). *P* values were calculated by ANOVA with Tukey's *post*-test: $^{*}P < 0.05$, $^{**}P < 0.01$.

chemotherapy alone based on ROS from the reaction of iron ion and Art, or PTT alone based on FeOOH@PNE exhibited a mild antitumour effect, their combination treatment achieved effective killing of cancer cells.

In vivo optical imaging

To investigate the biodistribution of our as-prepared nanoparticles *in vivo*, mice bearing 4T1 tumour were intravenously injected with FeOOH@PNE-RhB. After sacrificing mice at 1, 2, 4, 8 h post-injection, the *ex vivo* fluorescence imaging of the collected tumour, heart, liver, spleen, lung and kidney was observed. As shown in Fig. 8A, the FeOOH@PNE-RhB nanoparticles mainly accumulated in tumour, live, lung and kidney, and the fluorescence signal of tumours enhanced gradually within 8 hours, indicating that the nanoparticles can be passively targeted to the tumour site *via* EPR effect. To further inspect the tumour targeting of the nanoparticles, infrared thermal imaging analysis was carried out by intravenous

injection of the nanoparticles in the mice bearing 4T1 tumour, followed by the irradiation with an 808 nm laser (2 W cm^{-2}) for 5 min. As shown in Fig. 8B, the PBS injected group exhibited a negligible increase in temperature after 5 min irradiation. However, the mice injected with FeOOH@PNE and FeOOH@PNE-Art presented significantly localised heating in the tumour region under the identical laser irradiation, convincing the specific tumour targeting of the as-prepared nanoparticles. Moreover, the surface temperature of tumour in FeOOH@PNE and FeOOH@PNE-Art injected mice was over 55 °C, which not only satisfied the needs of hyperthermia of tumour, but also could quickly introduce cancer cell necrosis.

In vivo therapeutic performance

30 mice were randomly divided into six groups (n = 5 per group), involving PBS, PBS + laser, Art, FeOOH@PNE-Art, FeOOH@PNE + laser and FeOOH@PNE-Art + laser. After 8 h of intravenous administration, the treated mice received an irradiation of an 808 nm laser (2 W cm^{-2}) for 5 min or no irradiation each day of the first seven days of treatment. The digital photos, tumour volume and body weight of the treated mice were monitored within 14 days for comprehensive evaluation of the *in vivo* therapeutic effects. Digital photos and tumour relative volume curve (Fig. 9A–C) revealed that tumour continued to grow during the whole treatment period in PBS and PBS + laser groups. Compared with control group (PBS), free Art group and FeOOH@PNE-Art group showed a certain degree of inhibition of tumour growth. Since the FeOOH@PNE-Art nanoparticles were readily more internalised by cancer cells than free Art and the iron ion released from the nanoparticles facilitated the ROS generation *via* reaction of Fe^{2+} and Art, FeOOH@PNE-Art group have a higher antitumour efficacy than Art group. A significant inhibitory rate was observed for the FeOOH@PNE + laser group at 7 days, suggesting that tumour growth could be obviously inhibited by the photothermal therapy of the FeOOH@PNE. However, it was worth noting that PTT alone of FeOOH@PNE could not accomplish complete ablation of tumour and tumour in FeOOH@PNE + laser group began to grow again after terminating PTT. Due to enhanced drug delivery[58] and ROS generation by PTT,[59] in FeOOH@PNE-Art + laser group, the tumours were thoroughly eliminated after 7 days of treatment and no tumour recurrence was found in 30 days after treatment, manifesting the very high efficacy of combination therapy.

To further investigate the therapeutic effects of each group, H&E staining of tumour sections were performed after 4 days' treatment (Fig. 9E). Compared with the control (PBS group), free Art, FeOOH@PNE-Art, FeOOH@PNE + laser and FeOOH@PNE-Art + laser group showed a sequentially enhanced injury of tumour tissue, which was in agreement with the tumour growth curve. The outstanding efficacy of FeOOH@PNE-Art + laser group can be attributed to the enhanced ROS generation by heating effects of the nanoparticles under laser irradiation.

Finally, the toxic side effects of the as-prepared nanoparticles *in vivo* were investigated by body weight change and H&E staining analysis of the major organs. No significant change of body weight could be observed in all groups, implicating that

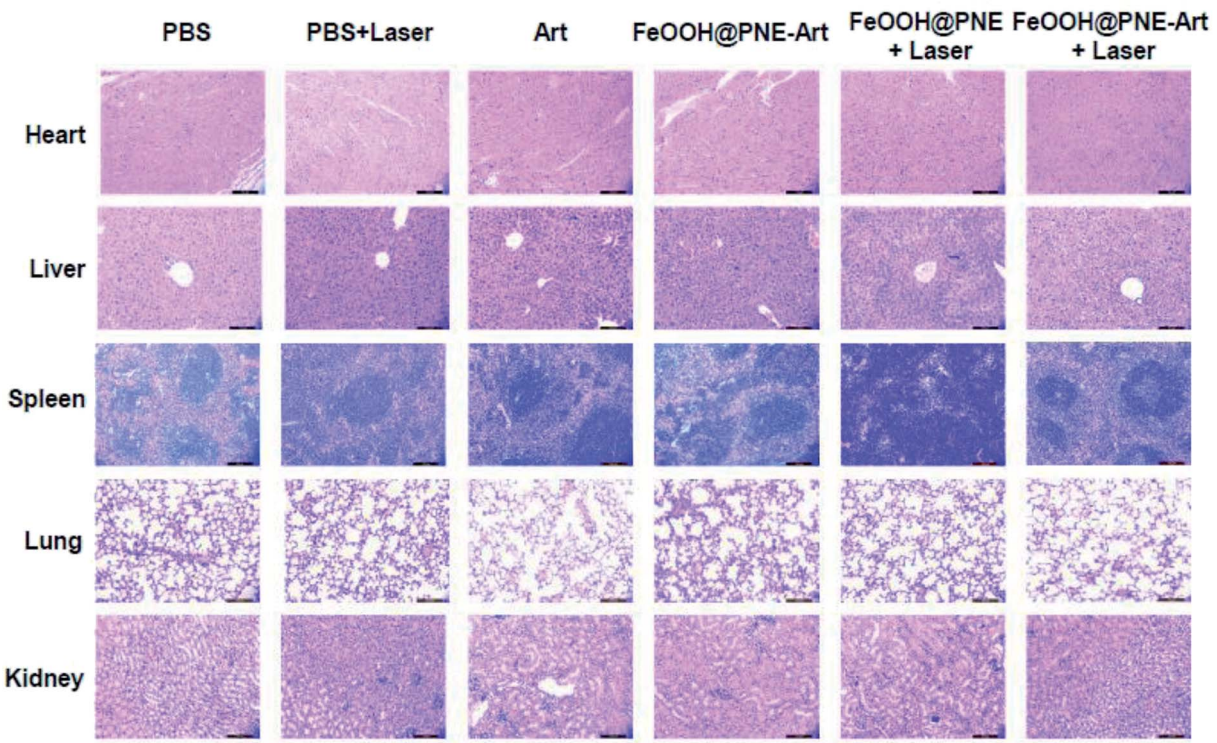

Fig. 10 H&E stained slices of major organs acquired from various treatment groups. The mice were dissected 4 days after intravenous injection for harvesting their organs (scale bar, 100 μm).

healthy status of mice is hardly influenced by the administration of the nanoparticles during assessment (Fig. 9D). H&E staining images (Fig. 10) revealed that no obvious cell damage could be observed on the main organs (heart, liver, spleen, lung and kidney), proving the good biocompatibility and safety of the FeOOH@PNE-Art nanoparticles.

Conclusions

We developed a tumour-specific FeOOH@PNE-Art nanoparticles for photothermal-chemical combination therapy of cancer. The inner fusiform FeOOH with low leakage of iron ions significantly enhanced the uptake efficiency of Art in tumour cells and decrease the Art toxicity to normal tissue, while the outer PNE acted as a photothermal coating, for the first time. The as-prepared FeOOH@PNE-Art nanoparticles exhibited a pH-responsive synchronous release of Art and iron ions, indicating that the tumour-specific acid microenvironment was conducive to enhancing Art and iron ions synchronous release locally. Besides ROS produced by the reaction of ferrous ions and Art, the released iron ions could also react with H_2O_2 in tumour microenvironment to generate hydroxyl radical. Moreover, since ROS generation could be enhanced at higher temperature, the ROS cytotoxicity was further promoted by photothermal effects under NIR irradiation. This strategy of local ROS generation has great potential to achieve tumour-specific killing. Although ROS-mediated chemotherapy alone or FeOOH@PNE-based PTT alone only offered a mild antitumour effect, their combination treatment acquired complete cure of tumours without observable side effects on normal tissues. Overall, our work presents a nanoplatform combining PTT and chemotherapy with high antitumour efficacy and low side effects, providing a promising method for clinical tumour therapy.

Conflicts of interest

There are no conflicts to declare.

Acknowledgements

This work was supported by the National Nature Science Foundation of China (81271689, 31271009, 31870986), the Program for New Century Excellent Talents in University, the Program for New Century Excellent Talents in Fujian Province University, and the Fundamental Research Funds for the Central Universities (20720150087).

References

1 C. H. Heldin, K. Rubin, K. Pietras and A. Ostman, High interstitial fluid pressure - an obstacle in cancer therapy, *Nat. Rev. Cancer*, 2004, **4**, 806–813.

2 R. V. J. Chari, M. L. Miller and W. C. Widdison, Antibody-drug conjugates: an emerging concept in cancer therapy, *Angew. Chem., Int. Ed.*, 2014, **53**, 3796–3827.

3 D. Luo, K. A. Carter, D. Miranda and J. F. Lovell, Chemophototherapy: an emerging treatment option for solid tumors, *Adv. Sci.*, 2017, **4**, 1600106.

4 X. X. Bi, H. L. Su, W. Shi, X. Liu, Z. He, X. M. Zhang, Y. N. Sun and D. T. Ge, BSA-modified poly(pyrrole-3-carboxylic acid) nanoparticles as carriers for combined chemo-photothermal therapy, *J. Mater. Chem. B*, 2018, **6**, 7877–7888.

5 W. Fan, B. Yung, P. Huang and X. Chen, Nanotechnology for multimodal synergistic cancer therapy, *Chem. Rev.*, 2017, **117**, 13566–13638.

6 A. Ramazani, M. Keramati, H. Malvandi, H. Danafar and H. K. Manjili, Preparation and in vivo evaluation of anti-plasmodial properties of artemisinin-loaded PCL–PEG–PCL nanoparticles, *Pharm. Dev. Technol.*, 2017, **23**, 911.

7 Y. K. Wong, C. Xu, K. A. Kalesh, Y. He, Q. Lin, W. S. F. Wong, H. M. Shen and J. Wang, Artemisinin as an anticancer drug: recent advances in target profiling and mechanisms of action, *Med. Res. Rev.*, 2017, **37**, 1492–1517.

8 A. Blessing, Design of drug delivery systems containing artemisinin and its derivatives, *Molecules*, 2017, **22**, 323.

9 J. Chen, W. Zhang, M. Zhang, Z. Guo, H. Wang, M. He, P. Xu, J. Zhou, Z. Liu and Q. Chen, Mn(II) mediated degradation of artemisinin based on Fe_3O_4@$MnSiO_3$-FA nanospheres for cancer therapy in vivo, *Nanoscale*, 2015, **7**, 12542–12551.

10 N. P. Singh and H. C. Lai, Artemisinin induces apoptosis in human cancer cells, *Anticancer Res.*, 2004, **24**, 2277–2280.

11 H. Zhang, Q. Chen, X. Zhang, X. Zhu, J. Chen, H. Zhang, L. Hou and Z. Zhang, An intelligent and tumor-responsive Fe^{2+} donor and Fe^{2+}-dependent drugs cotransport system, *ACS Appl. Mater. Interfaces*, 2016, **8**, 33484–33498.

12 N. Klonis, D. J. Creek and L. Tilley, Iron and heme metabolism in plasmodium falciparum and the mechanism of action of artemisinins, *Curr. Opin. Microbiol.*, 2013, **16**, 722–727.

13 A. Ganguli, D. Choudhury, S. Datta, S. Bhattacharya and G. Chakrabarti, Inhibition of autophagy by chloroquine potentiates synergistically anti-cancer property of artemisinin by promoting ROS dependent apoptosis, *Biochimie*, 2014, **107**, 338–349.

14 N. Shterman, B. Kupfer and C. Moroz, Comparison of transferrin receptors, iron content and isoferritin profile in normal and malignant human breast cell lines, *Pathobiology*, 1991, **59**, 19–25.

15 S. R. Meshnick, Y. Z. Yang, V. Lima, F. Kuypers, S. Kamchonwongpaisan and Y. Yuthavong, Iron-dependent free radical generation from the antimalarial agent artemisinin (qinghaosu), *Antimicrob. Agents Chemother.*, 1993, **37**, 1108–1114.

16 Y. X. Ding, J. X. Wan, Z. H. Zhang, F. Wang, J. Guo and C. C. Wang, Localized Fe(II)-induced cytotoxic reactive oxygen species generating nanosystem for enhanced anticancer therapy, *ACS Appl. Mater. Interfaces*, 2018, **10**, 4439–4449.

17 D. D. Wang, J. J. Zhou, R. H. Chen, R. H. Shi, C. L. Wang, J. Lu, G. Z. Zhao, G. L. Xia, S. Zhou, Z. B. Liu, H. B. Wang, Z. Guo and Q. W. Chen, Core–shell metal-organic frameworks as Fe^{2+} suppliers for Fe^{2+}-mediated cancer

therapy under multimodality imaging, *Chem. Mater.*, 2017, **29**, 3477–3489.

18 J. Chen, Z. Guo, H. B. Wang, J. J. Zhou, W. J. Zhang and Q. W. Chen, Multifunctional mesoporous nanoparticles as pH-responsive Fe^{2+} reservoirs and artemisinin vehicles for synergistic inhibition of tumor growth, *Biomaterials*, 2014, **35**, 6498–6507.

19 D. D. Wang, J. J. Zhou, R. H. Chen, R. H. Shi, G. L. Xia, S. Zhou, Z. B. Liu, N. Q. Zhang, H. B. Wang and Z. Guo, Magnetically guided delivery of DHA and Fe ions for enhanced cancer therapy based on pH-responsive degradation of DHA-loaded Fe_3O_4@C@MIL-100(Fe) nanoparticles, *Biomaterials*, 2016, **107**, 88–101.

20 T. Efferth, A. Benakis, M. R. Romero, M. Tomicic, R. Rauh, D. Steinbach, R. Hafer, T. Stamminger, F. Oesch, B. Kaina and M. Marschall, Enhancement of cytotoxicity of artemisinins toward cancer cells by ferrous iron, *Free Radical Biol. Med.*, 2004, **37**, 998–1009.

21 Y. Wang, Y. X. Han, Y. Y. Yang, J. C. Yang, X. N. Guo, J. N. Zhang, L. Pan, G. H. Xia and B. A. Chen, Effect of interaction of magnetic nanoparticles of Fe_3O_4 and artesunate on apoptosis of K562 cells, *Int. J. Nanomed.*, 2011, **6**, 1185–1192.

22 B. A. Aderibigbe, Design of drug delivery systems containing artemisinin and its derivatives, *Molecules*, 2017, **22**, 323.

23 U. N. Pan, P. Sanpui, A. Paul and A. Chattopadhyay, Synergistic anticancer potential of artemisinin when loaded with 8-hydroxyquinoline-surface complexed-zinc ferrite magnetofluorescent nanoparticles and albumin composite, *ACS Appl. Bio Mater.*, 2018, **1**, 1229.

24 V. P. Chauhan and R. K. Jain, Strategies for advancing cancer nanomedicine, *Nat. Mater.*, 2013, **12**, 958–962.

25 X. Huang, X. Teng, D. Chen, F. Tang and J. He, The effect of the shape of mesoporous silica nanoparticles on cellular uptake and cell function, *Biomaterials*, 2010, **31**, 438–448.

26 Y. Wang, Y. Xiao and R. K. Tang, Spindle-like polypyrrole hollow nanocapsules as multifunctional platforms for highly effective chemo-photothermal combination therapy of cancer cells in vivo, *Chem.–Eur. J.*, 2014, **20**, 11826–11834.

27 H. Seonki, K. Jihoon, N. Y. Suk, P. Junghong, K. Sunjin, S. Kaushik, I. Guu-Il, H. D. Keun, K. W. Jong and L. Haeshin, Poly(norepinephrine): ultrasmooth material-independent surface chemistry and nanodepot for nitric oxide, *Angew. Chem., Int. Ed.*, 2013, **125**, 9357–9361.

28 S. M. Kang, S. Park, D. Kim, S. Y. Park, R. S. Ruoff and H. Lee, Simultaneous reduction and surface functionalization of graphene oxide by mussel-inspired chemistry, *Adv. Funct. Mater.*, 2011, **21**, 108–112.

29 H. Lee, S. M. Dellatore, W. M. Miller and P. H. Messersmith, Mussel-inspired surface chemistry for multifunctional coatings, *Science*, 2007, **318**, 426–430.

30 C. E. Brubaker, H. Kissler, L. J. Wang, D. B. Kaufman and P. B. Messersmith, Biological performance of mussel-inspired adhesive in extrahepatic islet transplantation, *Biomaterials*, 2010, **31**, 420–427.

31 S. Hong, Y. S. Na, S. Choi, I. T. Song and W. Y. Kim, Non-covalent self-assembly and covalent polymerization co-contribute to polydopamine formation, *Adv. Funct. Mater.*, 2012, **22**, 4711–4717.

32 Y. Liu, G. Q. Zhou, Z. Liu, M. Y. Guo, X. M. Jiang, M. B. Taskin, Z. Y. Zhang, J. Liu, J. L. Tang, R. Bai, F. Besenbacher and M. L. Chen, Mussel inspired polynorepinephrine functionalized electrospun polycaprolactone microfibers for muscle regeneration, *Sci. Rep.*, 2017, **7**, 8197.

33 M. A. F. Nejad, F. Ghasemi and M. R. H. Nezhad, A wide-color-varying ratiometric nanoprobe for detection of norepinephrine in urine samples, *Anal. Chim. Acta*, 2018, **1039**, 124–131.

34 D. Yang, X. Y. Wang, Q. H. Ai, J. F. Shi and Z. Y. Jiang, Performance comparison of immobilized enzyme on the titanate nanotube surfaces modified by poly(dopamine) and poly(norepinephrine), *RSC Adv.*, 2015, **5**, 42461.

35 J. Chen, R. P. Liang, X. N. Wang and J. D. Qiu, A norepinephrine coated magnetic molecularly imprinted polymer for simultaneous multiple chiral recognition, *J. Chromatogr. A*, 2015, **1409**, 268–276.

36 T. Iwasaki, Y. Tamai, M. Yamamoto, T. Taniquchi, K. Kishikawa and M. Kohri, Melanin precursor influence on structural colors from artificial melanin particles: polyDOPA, polydopamine, and polynorepinephrine, *Langmuir*, 2018, **34**, 11814–11821.

37 M. B. Taskin, R. Xu, H. Zhao, X. Wang, M. Dong, F. Beaenbacher and M. Chen, Poly(norepinephrine) as a functional bio-interface for neuronal differentiation on electrospun fibers, *Phys. Chem. Chem. Phys.*, 2015, **17**, 9446–9453.

38 X. M. Jiang, Y. F. Li, Y. Liu, C. Y. Chen and M. L. Chen, Selective enhancement of human stem cell proliferation by mussel inspired surface coating, *RSC Adv.*, 2016, **6**, 60206.

39 J. Chen, R. P. Liang, L. L. Wu and J. D. Qiu, One-step preparation and application of mussel-inspired poly(norepinephrine)-coated polydimethylsiloxane microchip for separation of chiral compounds, *Electrophoresis*, 2016, **37**, 1676–1684.

40 S. H. Yang, S. M. Kang, K. B. Lee, T. D. Chung, H. Lee and I. S. Choi, Mussel-inspired encapsulation and functionalization of individual yeast cells, *J. Am. Chem. Soc.*, 2011, **133**, 2795–2797.

41 B. Wang, G. Wang, B. Zhao, J. Chen, X. Zhang and R. Tang, Antigenically shielded universal red blood cells by polydopamine-based cell surface engineering, *Chem. Sci.*, 2014, **5**, 3463–3468.

42 X. J. Liang, Y. X. Yang, X. N. Liu, H. Zhu, H. P. Ying, Z. Y. Zhou and Y. R. Chen, Study on the synthesis of β-FeOOH by the microemulsion method, *Russ. J. Inorg. Chem.*, 2008, **53**, 367–371.

43 D. D. Wang, J. J. Zhou, R. H. Chen, R. H. Shi, G. Z. Zhao, G. L. Xia, R. Li, Z. B. Liu, J. Tian, H. J. Wang, Z. Guo, H. B. Wang and Q. W. Chen, Controllable synthesis of dual-MOFs nanostructures for pH-responsive artemisinin delivery, magnetic resonance and optical dual-model imaging-guided chemo/photothermal combinational cancer therapy, *Biomaterials*, 2016, **100**, 27–40.

44 J. Chen, Z. Guo, H. B. Wang, J. J. Zhou, W. J. Zhang and Q. W. Chen, Multifunctional mesoporous nanoparticles as pH-responsive Fe^{2+} reservoirs and artemisinin vehicles for synergistic inhibition of tumor growth, *Biomaterials*, 2014, **35**, 6498–6507.

45 X. Liu, H. L. Su, W. Shi, Y. Liu, Y. N. Sun and D. T. Ge, Functionalized poly(pyrrole-3-carboxylic acid) nanoneedles for dual-imaging guided PDT/PTT combination therapy, *Biomaterials*, 2018, **167**, 177–190.

46 J. Tu, T. X. Wang, W. Shi, G. S. Wu, X. H. Tian, Y. H. Wang, D. T. Ge and L. Ren, Multifunctional ZnPc-loaded mesoporous silica nanoparticles for enhancement of photodynamic therapy efficacy by endolysosomal escape, *Biomaterials*, 2012, **33**, 7903–7914.

47 D. Hanahan and R. A. Weinberg, Hallmarks of cancer: the next generation, *Cell*, 2011, **144**, 646–674.

48 C. Zhang, W. Bu, D. Ni, S. Zhang, Q. Li, Z. Yao, J. Zhang, H. Yao, Z. Wang and J. Shi, Synthesis of iron nanometallic glasses and their application in cancer therapy by a localized fenton reaction, *Angew. Chem., Int. Ed.*, 2016, **55**, 2101–2106.

49 S. H. Crayton and A. Tsourkas, pH-titratable superparamagnetic iron oxide for improved nanoparticle accumulation in acidic tumor microenvironments, *ACS Nano*, 2011, **5**, 9592–9601.

50 Z. Tang, H. Zhang, Y. Liu, D. Ni, H. Zhang, J. Zhang, Z. Yao, M. He, J. Shi and W. Bu, Antiferromagnetic pyrite as the tumor microenvironment-mediated nanoplatform for self-enhanced tumor imaging and therapy, *Adv. Mater.*, 2017, **29**, 1701683.

51 L. Wang, M. Huo, Y. Chen and J. Shi, Iron-engineered mesoporous silica nanocatalyst with biodegradable and catalytic framework for tumor-specific therapy, *Biomaterials*, 2018, **163**, 1–13.

52 P. Hu, T. Wu, W. Fan, L. Chen, Y. Liu, D. Ni, W. Bu and J. Shi, Near infrared-assisted fenton reaction for tumor-specific and mitochondrial DNA-targeted photochemotherapy, *Biomaterials*, 2017, **141**, 86–95.

53 Y. Dai, Z. Yang, S. Cheng, Z. Wang, R. Zhang, G. Zhu, Z. Wang, B. C. Yung, R. Tian, O. Jacobson, C. Xu, Q. Ni, J. Song, X. Sun, G. Niu and X. Chen, Toxic reactive oxygen species enhanced synergistic combination therapy by self-assembled metal-phenolic network nanoparticles, *Adv. Mater.*, 2018, **30**, 1704877.

54 Z. Shen, J. Song, B. C. Yung, Z. Zhou, A. Wu and X. Chen, Emerging strategies of cancer therapy based on ferroptosis, *Adv. Mater.*, 2018, **30**, 1704007.

55 M. Lopez-Lazaro, Dual role of hydrogen peroxide in cancer: possible relevance to cancer chemoprevention and therapy, *Cancer Lett.*, 2007, **252**, 1–8.

56 M. Huo, L. Wang, Y. Chen and J. Shi, Tumor-selective catalytic nanomedicine by nanocatalyst delivery, *Nat. Commun.*, 2017, **8**, 357.

57 Z. Luo, K. Cai, Y. Hu, J. Li, X. Ding, B. Zhang, D. Xu, W. Yang and P. Liu, Redox-responsive molecular nanoreservoirs for controlled intracellular anticancer drug delivery based on magnetic nanoparticles, *Adv. Mater.*, 2012, **24**, 431–435.

58 D. D. Luo, K. A. Carter, E. A. G. Molins, N. L. Straubinger, J. Geng, S. Shao, W. J. Jusko, R. M. Straubinger and J. F. Lovell, Pharmacokinetics and pharmacodynamics of liposomal chemophototherapy with short drug-light intervals, *J. Controlled Release*, 2019, **297**, 39–47.

59 H. H. Wu, K. M. Cheng, Y. He, Z. Y. Li, H. L. Su, X. M. Zhang, Y. N. Sun, W. Shi and D. T. Ge, Fe_3O_4-based multifunctional nanospheres for amplified magnetic targeting photothermal therapy and Fenton reaction, *ACS Biomater. Sci. Eng.*, 2019, **5**, 1045–1056.